A spawning particle filter for defocused moving target detection in GNSS-based passive radar

ZENG Hongcheng[1,2], DENG Jiadong[1], WANG Pengbo[1], ZHOU Xinkai[1],
YANG Wei[1], and CHEN Jie[1,*]

1. School of Electronic and Information Engineering, Beihang University, Beijing 100191, China; 2. National Key Laboratory of Science and Technology on Space Microwave, China Academy of Space Technology, Xi'an 710000, China

Abstract: Global Navigation Satellite System (GNSS)-based passive radar (GBPR) has been widely used in remote sensing applications. However, for moving target detection (MTD), the quadratic phase error (QPE) introduced by the non-cooperative target motion is usually difficult to be compensated, as the low power level of the GBPR echo signal renders the estimation of the Doppler rate less effective. Consequently, the moving target in GBPR image is usually defocused, which aggravates the difficulty of target detection even further. In this paper, a spawning particle filter (SPF) is proposed for defocused MTD. Firstly, the measurement model and the likelihood ratio function (LRF) of the defocused point-like target image are deduced. Then, a spawning particle set is generated for subsequent target detection, with reference to traditional particles in particle filter (PF) as their parent. After that, based on the PF estimator, the SPF algorithm and its sequential Monte Carlo (SMC) implementation are proposed with a novel amplitude estimation method to decrease the target state dimension. Finally, the effectiveness of the proposed SPF is demonstrated by numerical simulations and preliminary experimental results, showing that the target range and Doppler can be estimated accurately.

Keywords: Global Navigation Satellite System (GNSS)-based passive radar (GBPR), defocused target, moving target detection (MTD), likelihood ratio function (LRF), spawning particle filter (SPF).

1. Introduction

Recently, the Global Navigation Satellite System (GNSS) signals have been receiving particular attention in passive radar, due to their permanent global coverage, ease for synchronization and abundant satellite resources

[1−5]. As a powerful remote sensing tool, the GNSS-based passive radar (GBPR) has been widely studied for synthetic aperture radar (SAR) [5−7], change detection [8] and moving target detection (MTD) [9−11], including ship targets [11−13] and aerial targets [14].

Although the GBPR system has many advantages compared with other illuminators, its low power level is a crucial issue [15]. For SAR imaging, huge process gain can be achieved with long coherent integration time (CIT). However, for MTD, it is challenging to obtain enough signal-to-noise ratio (SNR) for a satisfactory detection probability with a small false alarm rate. As the target motion is unknown, Doppler frequency migration (DFM) and range cell migration (RCM) caused by target motion are difficult to be compensated [16,17]. Usually, the cross-ambiguity function is widely used to obtain the delay-Doppler map, but it is only applicable in short time case [18]. In order to increase the CIT, both Radon Fourier transform (RFT)-based [19−21] and Radon fractional Fourier transform (FrFT)-based [22] methods are proposed, which can focus the moving target in the range-Doppler (RD) domain and the CIT can be up to tens of seconds theoretically. In addition, a new strategy with hybrid coherent and noncoherent integration technique is proposed [9]. However, in the abovementioned methods, Doppler rate searching or estimation is required to compensate the quadratic phase error (QPE) caused by target motion, which is time-consuming or even not working as the SNR is quite low.

In general, the QPE caused by Doppler rate can defocus the target and lead to reduction in image SNR; but if the CIT is short enough (several seconds), these effects will not be serious. Based on this consideration, the non-threshold method can be used for MTD, such as track before detection (TBD) [23,24]. Using a sequence of system measurements, the TBD can potentially detect mov-

ing targets with a much lower SNR than traditional methods. A few TBD algorithms have been developed based on the recursive Bayesian estimator, such as the particle filter (PF) [25−27], the probability hypothesis density (PHD) filter [28,29], and the multi-Bernoulli filter [30,31]. Due to its simple implementation and good performance at low SNR conditions, the PF and its variations have been widely used [24]. The PF and its implementation were firstly introduced for low SNR point target detection [25,27]. Moreover, detailed explanation, performance analysis, and the Cramer-Rao lower bound of PF were also presented [24], and modified PFs were proposed for detection of maneuvering targets, multiple targets and extended targets [32−34]. Further improvements were made on the PF in radar signal processing [23,35]. These PFs are mainly used to detect point targets or extended targets. In GBPR, small moving targets can be focused into a point-like target in RD plane in theory. However, in practice, moving targets are normally defocused, as it is difficult to completely compensate the QPE. Moreover, the state-of-art PFs are not suitable for defocused MTD, and even the likelihood ratio function (LRF) of the point target or the extended target is not suitable. Therefore, to detect the defocused moving target in GBPR, it is crucial to study the improved PF-based algorithm.

Our research in this work is focused on the defocused MTD using a sequence of GBPR image frames, and a novel spawning PF (SPF) is proposed with a modified LFR model and an amplitude estimation. Firstly, the LRF model in the defocused target of RD image is developed. Then, the spawning particle concept is introduced to calculate the modified LRF model. The spawning particles are born by a uniform distribution with reference to each traditional particle as their parent. After that, an amplitude estimation is proposed based on spawning particles, which can avoid sampling in amplitude dimension. Finally, the SPF and its sequential Monte Carlo (SMC) implementation are presented, including initializing, LRF with amplitude estimation, existing spawning particles, newborn spawning particles, mixed spawning particle set, resampling, and target state estimation.

This paper is organized as follows. Analysis of the moving target signal in GBPR is presented in Section 2, including the Doppler characteristic and RD image results. Then, in Section 3, the measurement model for defocused moving targets is presented, followed by the LRF modeling. In Section 4, the proposed SPF algorithm using a sequence of RD image frames is derived in detail, with its SMC implementation. In order to testify the effectiveness of the SPF, numerical simulations and preliminary experimental results are provided in Section 5. Section 6 concludes the paper.

2. Analysis of moving target signal in GBPR system

2.1 Doppler characteristic analysis

Fig. 1 shows the general geometry of a GBPR with a moving target, where the origin O is set to be the radar receiver, while the X- and Y- axes point to the East and North directions, respectively. Assume that the moving target M is located at $\boldsymbol{P}_{\text{tar}}(X_M, Y_M, Z_M)$ with a constant velocity $\boldsymbol{V}_{\text{tar}}(V_{Mx}, V_{My}, V_{Mz})$, while the transmitter is located at $\boldsymbol{P}_{\text{Tran}}(X_T, Y_T, Z_T)$ with a velocity vector $\boldsymbol{V}_{\text{Tran}}(V_{Tx}, V_{Ty}, V_{Tz})$. $R_T(t)$, $R_R(t)$, and $R_D(t)$ denote the instantaneous transmitter slant range, receiver slant range and direct range, respectively.
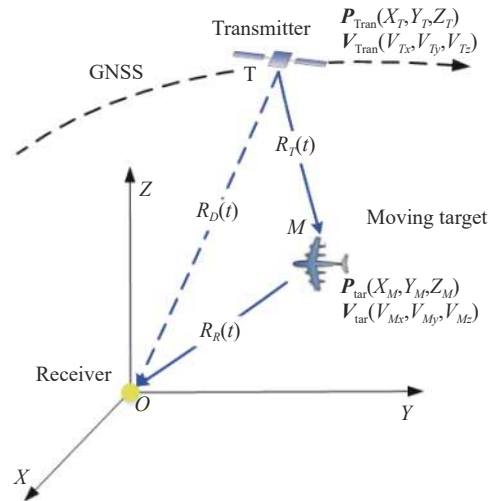

Fig. 1　General geometry of GBPR with a moving target

Then, the range history $R(t)$ variation with time t is

$$R(t) = R_T(t) + R_R(t) = R_{\text{ref}} + \lambda f_d t + \frac{\lambda}{2} f_r t^2 \qquad (1)$$

where λ is the signal wavelength, and R_{ref}, f_d, and f_r denote reference range, Doppler centroid, and Doppler rate, respectively. f_d and f_r can be derived as

$$\begin{cases} f_d = \dfrac{1}{\lambda} \dfrac{\mathrm{d}R(t)}{\mathrm{d}t}\bigg|_{t=0} = f_{d0} + f_{dm} \\ f_r = \dfrac{1}{\lambda} \dfrac{\mathrm{d}^2R(t)}{\mathrm{d}t^2}\bigg|_{t=0} = f_{r0} + f_{rm} \end{cases} \qquad (2)$$

where f_{d0} and f_{r0} denote the Doppler history introduced by the system motion, and f_{dm} and f_{rm} are the corresponding variations introduced by target motion. As the coordinates of the transmitter and receiver are known, it is easy to remove f_{d0} and f_{r0} terms from the synchronization outputs. Therefore, to simplify the subsequent derivation, the Doppler history only caused by the system motion is not considered in the following. The unknown f_{dm} can cause Doppler shift and image defocusing, but it can be estimated and compensated by the RFT method. The unknown f_{rm} can cause image defocusing and can be esti-

mated by techniques such as peak value searching, if the image SNR is large enough [14].

Using the GNSS satellite parameters (refer to Subsection 5.1), the variations of f_{rm} are shown in Fig. 2, as the f_{rm} term is important for focusing. In Fig. 2(a), moving target A is located at (1,1,0.3) km with a velocity 100 m/s, and at this condition, the f_{rm} is about 27.05±0.1 Hz/s. As depicted in Fig. 2(b), moving target B is located at (100,100,8) km with a velocity 300 m/s, and at this condition, f_{rm} is about 2.5±0.3 Hz/s. In Fig. 2, the X-axis is the angle between target velocity and the Y-axis in Fig. 1. As shown in Fig. 2, f_{rm} is relatively small, but it cannot be ignored, because the QPE and the length of Doppler frequency spread caused by f_{rm} are sufficiently large.

(a) Target A

(b) Target B

——: Satellite SVN #10; ——: Satellite SVN #18;
••••: Satellite SVN #24.
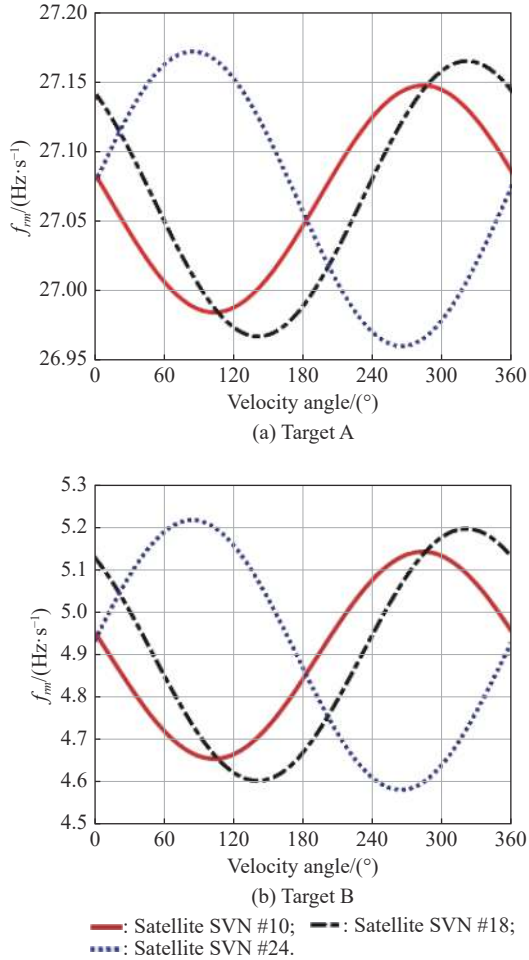
Fig. 2 Variation of f_{rm} caused by target motion in different geometric configurations with targets A and B

## 2.2　RD image results of moving target

In order to obtain enough image SNR for MTD, long CIT processing in GBPR is necessary. A modified RFT with Doppler rate estimation was proposed in [36], which can focus the moving target (point target) in the RD domain:

$$S_o(f_v,R)\big|_{\hat{f}_r=f_{rm}} = A \sum_{m=-N_a/2}^{N_a/2-1} C[R-R_{\text{ref}}+\lambda(f_v-f_{dm})mT_p]\cdot$$

$$\exp\{j2\pi(f_v-f_{dm})mT_p\}\big|_{\hat{f}_r=f_{rm}} \qquad (3)$$

where A is the amplitude factor, $C(\cdot)$ is the normalized auto-correlation function of GNSS transmitted signal, T_p is the signal period, N_a is the azimuth sample number, f_v is the Doppler frequency, and $\hat{f}_r$ is the estimated Doppler rate. Obviously, the maximum output occurs at the position of target motion parameters $(R_{\text{ref}}, f_{dm}, f_{rm})$. As shown in (3), three dimensional (3D) parameter searching is performed in modified RFT, which is time-consuming. Moreover, although many solutions can provide the Doppler rate and its phase error, such as the amplitude auto-focus method, their effectiveness is highly dependent on the image SNR, and they may even fail if the image SNR is too low. Therefore, RD 2D parameters searching is normally used, and the output will be

$$S_o(f_v,R) = A \sum_{m=-N_a/2}^{N_a/2-1} C[R-R_{\text{ref}}+\lambda(f_v-f_{dm})mT_p]\cdot$$

$$\exp\{j2\pi(f_v-f_{dm})mT_p\}\cdot\exp\{j\pi f_{rm}(mT_p)^2\} \qquad (4)$$

where the range-curvature term in $C(\cdot)$ is ignored, as it is much smaller than one range cell. As shown in (4), the moving target is defocused at the RD plane due to the QPE. Actually, the uncompensated f_{rm} term can only lead to image defocusing in the Doppler domain, as the range-curvature is ignored. The signal expansion length in the Doppler domain is $f_{rm}N_a/\text{PRF}$, and the corresponding Doppler cell number is $f_{rm}(N_a/\text{PRF})^2$, where PRF denotes the equivalent pulse repetition frequency of GNSS signals. Based on the signal model in (3) and (4), the ideal results with and without Doppler rate compensation are shown in Fig. 3 (f_{rm}=0.2 Hz/s, N_a/PRF = 5 s). As shown in Fig. 3(b), the moving target signal is defocused in the Doppler domain.
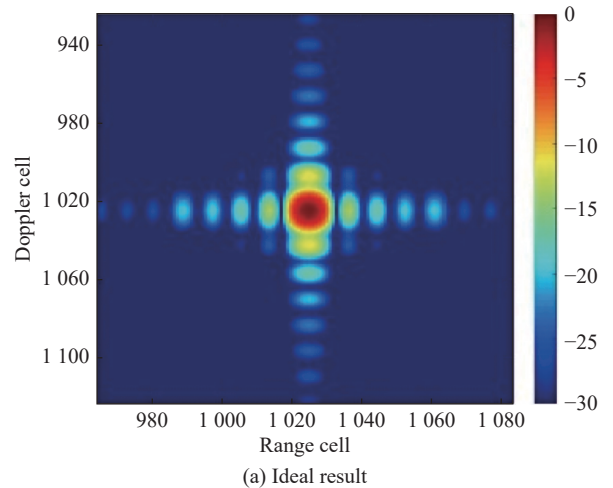
(a) Ideal result
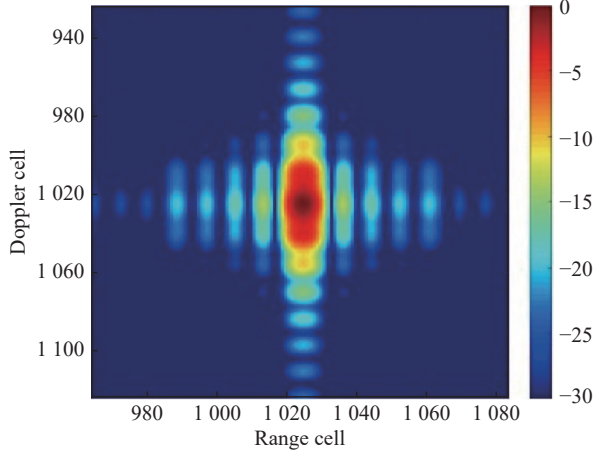
(b) Result without $f_{\rm rm}$ compensation

Fig. 3   Interpolation point target result processed by RFT

3. Measurement model and LRF of defocused moving target

In GBPR, moving targets can be focused in RD plane by the modified RFT. However, due to its low image SNR, it is really difficult to estimate the f_{rm} term caused by target motion. As a result, the moving target is usually defocused, and the traditional track after the detection method does not work. In this paper, the PF-based method is used for the defocused MTD.

3.1 Measurement model

Assume the kth frame image is the measurement z_k, and each cell in this frame can be modelled as

$$z_k = \left\{ z_k^{(i,j)}, \ i = 1, 2, \cdots, N_f, \ j = 1, 2, \cdots, N_r \right\} \quad (5)$$

where N_f and N_r denote the number of Doppler cell and range cell, respectively. For each cell, there are only two states: target exists or no target. Therefore, the random variable $E_k \in \{e, \bar{e}\}$ can be used to indicate whether the target exists at the kth frame or at time k. Normally, there is only one target in a imaging cell. Therefore, the measurement model is

$$z_k^{(i,j)} = \begin{cases} g_k^{(i,j)}(\boldsymbol{x}_k) + v_k^{(i,j)}, & E_k = e \\ v_k^{(i,j)}, & E_k = \bar{e} \end{cases} \quad (6)$$

where $v_k^{(i,j)}$ is the noise in the (i,j)th cell, which is normally independent zero-mean Gaussian distributed with variance σ^2. $\boldsymbol{x}_k$ is the target state vector at time k, and can be modelled as $\boldsymbol{x}_k = [A_k, R_k, f_{d,k}, f_{r,k}]$, where A_k, R_k, $f_{d,k}$, and $f_{r,k}$ denote the amplitude, target reference range, target Doppler frequency and target Doppler rate at time k.

$g_k^{(i,j)}(\cdot)$ is the point target response function, and based on the signal model in (4), it is

$$g_k^{(i,j)}(\boldsymbol{x}_k) = A_k \sum_{m=-N_A/2}^{N_A/2-1} C\left[R^j - R_k + \lambda\left(f^i - f_{d,k}\right)mT_p\right] \cdot$$

$$\exp\left\{j2\pi\left(f^i - f_{d,k}\right)mT_p\right\} \cdot \exp\left\{j\pi f_{r,k}(mT_p)^2\right\} \quad (7)$$

where R^j and f^i denote the range sampling sequence and frequency sampling sequence, and $R^j = R_{\rm ref} + (j - N_r/2)\Delta R$, $f^i = (i - N_f/2)\Delta f$, and ΔR and Δf are the range unit and doppler unit, respectively.

3.2 Modified LRF modelling

For the focused point target in a radar image, it is generally assumed that the intensity of each pixel follows the Rice distribution if target exists, or Rayleigh distribution if only noise is present [35]. Hence, the likelihood function in pixel (i,j) is

$$p\left(z_k^{(i,j)}|\boldsymbol{x}_k, e\right) = \frac{2z_k^{(i,j)}}{\sigma^2} I_0\left(\frac{2z_k^{(i,j)} g_{k,\rm ideal}^{(i,j)}(\boldsymbol{x}_k)}{\sigma^2}\right) \cdot$$

$$\exp\left\{-\frac{\left|z_k^{(i,j)}\right|^2 + \left|g_{k,\rm ideal}^{(i,j)}(\boldsymbol{x}_k)\right|^2}{\sigma^2}\right\}. \quad (8)$$

$$p\left(z_k^{(i,j)}|\bar{e}\right) = \frac{2z_k^{(i,j)}}{\sigma^2} \exp\left\{-\frac{\left|z_k^{(i,j)}\right|^2}{\sigma^2}\right\} \quad (9)$$

where $I_0(\cdot)$ is the zero-order Bessel function, $g_{k,\rm ideal}^{(i,j)}(\cdot)$ is the ideal point target response function as shown in (3). As the noise in each pixel is assumed to be independent, the likelihood function of the focused point target is a product over all of the contributions:

$$\begin{cases} p(z_k|\boldsymbol{x}_k, e) = \displaystyle\prod_{i=1}^{N_f}\prod_{j=1}^{N_r} p\left(z_k^{(i,j)}|\boldsymbol{x}_k, e\right) \\ p(z_k|\bar{e}) = \displaystyle\prod_{i=1}^{N_f}\prod_{j=1}^{N_r} p\left(z_k^{(i,j)}|\bar{e}\right) \end{cases}. \quad (10)$$

Therefore, the statistical LRF of the ideal point target is

$$L_{\rm ideal}(z_k|\boldsymbol{x}_k, e_k) = \frac{p(z_k|\boldsymbol{x}_k, e)}{p(z_k|\bar{e})} =$$

$$\prod_{i=1}^{N_f}\prod_{j=1}^{N_r}\exp\left\{-\frac{\left|g_{k,\rm ideal}^{(i,j)}(\boldsymbol{x}_k)\right|^2}{\sigma_n^2}\right\} I_0\left(\frac{2z_k^{(i,j)} g_{k,\rm ideal}^{(i,j)}(\boldsymbol{x}_k)}{\sigma^2}\right). \quad (11)$$

In addition, the azimuth profile of the focused ideal point target is in the form of a sinc function, and the GNSS signal has a particularly excellent autocorrelation

property. Thus, the energy of the focused target is mainly concentrated in the main lobe. To improve the computation efficiency, a sub-area can be used for the whole image to calculate the LRF:

$$L_{\text{ideal}}(z_k|\boldsymbol{x}_k, e_k) =$$

$$\prod_{i=1}^{N_{f\_s}} \prod_{j=1}^{N_{r\_s}} \exp\left\{-\frac{\left|g_{k,\text{ideal}}^{(i,j)}(\boldsymbol{x}_k)\right|^2}{\sigma_n^2}\right\} I_0\left(\frac{2z_k^{(i,j)} g_{k,\text{ideal}}^{(i,j)}(\boldsymbol{x}_k)}{\sigma^2}\right) \quad (12)$$

where N_{f_s} and N_{r_s} denote the size of the sub-area image in RD domain. Normally, a 5×5 sub-area is recommended, considering the tradeoff between efficiency and accuracy.

Based on the LRF in (12), the moving target can be detected using PF in the GBPR. However, for the defocused target, there is no suitable probability model to directly describe the likelihood function in each pixel, as the energy of the moving target can expand into multiple-pixel areas. Usually, the defocused target is an object which is born in proximity to its corresponding focused point target, and the energy expansion area is highly related to the position $(f_{d,k}, R_k)$. Assume the state vector of the defocused target is $\boldsymbol{y}_k$, the energy expansion of the defocused target can be modelled as $\boldsymbol{y}_k \sim p(\boldsymbol{y}_k|\boldsymbol{x}_k)$, where $p(\boldsymbol{y}_k|\boldsymbol{x}_k)$ is the probability density function (PDF) for state $\boldsymbol{x}_k$ transfer to state $\boldsymbol{y}_k$. Therefore, the likelihood function of the defocused target can be described as

$$p(\boldsymbol{z}_k|\boldsymbol{x}_k, e) = \int p(\boldsymbol{z}_k|\boldsymbol{y}_k, e) p(\boldsymbol{y}_k|\boldsymbol{x}_k) \, d\boldsymbol{y}_k. \quad (13)$$

In order to calculate the likelihood function in (13), the extent of target defocusing should be carefully examined. Normally, the second-order phase modulation caused by $f_{r,k}$ only lead to reduced amplitude and Doppler defocused, and the peak position of the defocused target is still $(f_{d,k}, R_k)$. Assume the supporting length of the target distribution in the Doppler domain is L_f and the Doppler slice of the defocused target is

$$g_k(f_{d,k} + y, R_k) = A_k \sum_{m=-N_A/2}^{N_A/2-1} C\left[\lambda(y \cdot \Delta f) mT_p\right] \cdot$$

$$\exp\{j2\pi(y \cdot \Delta f) mT_p\} \cdot \exp\{j\pi f_{r,k}(mT_p)^2\} \quad (14)$$

where $y = [-L_f/2, L_f/2]$. Generally, for the CA code in GBPR, the range resolution is around 150 m, but the range-curvature term is just several meters. The Doppler defocusing extent is $L_f = f_{r,k} \cdot (N_a/\text{PRF})^2$. Then, we have

$$\left|\lambda(y \cdot \Delta f) mT_p\right| \leqslant \lambda\left(\frac{L_f}{2} \cdot \Delta f\right) = \frac{\lambda}{2}|f_{r,k}|\left(\frac{N_a}{\text{PRF}}\right)^2 \ll \Delta R \quad (15)$$

which means the term in the range envelop $C(\cdot)$ in (14) is smaller than one range cell, and $C[\lambda(y \cdot \Delta f) mT_p] \approx 1$. Thus, (14) can be rewritten as

$$g_k(f_{d,k} + y, R_k) = A_k \sum_{m=-N_A/2}^{N_A/2-1} \exp\{j2\pi(y \cdot \Delta f) mT_p\} \cdot$$

$$\exp\{j\pi f_{r,k}(mT_p)^2\}. \quad (16)$$

The range slice of the defocused target is

$$g_k(f_{d,k}, R^j) = \left[A_k \sum_{m=-N_A/2}^{N_A/2-1} \exp\{j\pi f_{r,k}(mT_p)^2\}\right] \cdot C(R^j - R_k). \quad (17)$$

Therefore, the target will still be focused in the range domain, with only reduced amplitude. Based on the above analysis, Fig. 4 presents distribution of the defocused moving target. As shown in Fig. 4, based on the target state $\boldsymbol{x}_k = [A_k, R_k, f_{d,k}, f_{r,k}]$, the defocused target state $\boldsymbol{y}_k$ can be modelled as $[A_{k,y}, R_k, f_{d,k} + y\Delta f, f_{r,k}]$, where the amplitude $A_{k,y}$ is decided by $A_k, f_{r,k}$, and N_a.
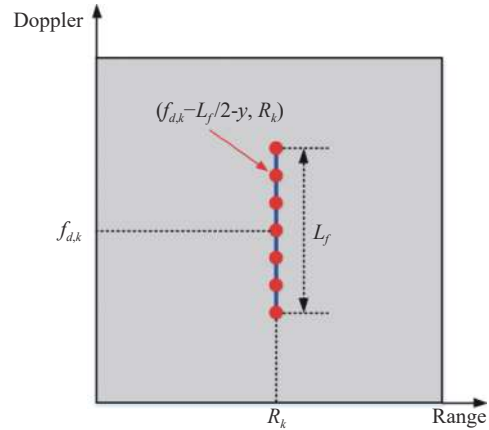

Fig. 4   Distribution of the defocused moving target

Then, the $p(\boldsymbol{z}_k|\boldsymbol{y}_k, e)$ in (13) can be calculated as

$$p\left(z_k^{(i+y,j)}|\boldsymbol{y}_k, e\right) = \frac{2z_k^{(i+y,j)}}{\sigma^2} I_0\left(\frac{2z_k^{(i+y,j)} g_{k,\text{ideal}}^{(i,j)}(f_{d,k} + y \cdot \Delta f, R_k)}{\sigma^2}\right) \cdot$$

$$\exp\left\{-\frac{\left|z_k^{(i+y,j)}\right|^2 + \left|g_{k,\text{ideal}}^{(i,j)}(f_{d,k} + y \cdot \Delta f, R_k)\right|^2}{\sigma^2}\right\}. \quad (18)$$

Normally, $p(\boldsymbol{y}_k|\boldsymbol{x}_k)$ can be set to the uniform distribution, based on the assumption that the target

energy distributes uniformly in the defocused area. Thus, the likelihood function in (13) can be calculated by

$$
p\left(z_k^{(i,j)}|\boldsymbol{x}_k,e\right) = \frac{1}{L_f}\int_{-L_f/2}^{L_f/2} \frac{2z_k^{(i+y,j)}}{\sigma^2}\cdot
$$

$$
I_0\left(\frac{2z_k^{(i+y,j)}g_{k,\,\mathrm{ideal}}^{(i,j)}\left(f_{d,k}+y\cdot\Delta f,R_k\right)}{\sigma^2}\right)\cdot
$$

$$
\exp\left\{-\frac{\left|z_k^{(i+y,j)}\right|^2 + \left|g_{k,\,\mathrm{ideal}}^{(i,j)}\left(f_{d,k}+y\cdot\Delta f,R_k\right)\right|^2}{\sigma^2}\right\}\mathrm{d}y. \quad (19)
$$

Same as (8), the intensity of a noise-only pixel is still Rayleigh distribution. Finally, based on (8), (10), (11), and (19), the statistical LRF of the defocused target can be modelled as

$$
L_{\mathrm{def}}\left(z_k|\boldsymbol{x}_k,e_k\right) =
$$

$$
\prod_{i=1}^{N_{f,s}}\prod_{j=1}^{N_{r,s}} \frac{1}{L_f}\int_{-L_f/2}^{L_f/2} \frac{z_k^{(i+y,j)}}{z_k^{(i,j)}} I_0\left(\frac{2z_k^{(i+y,j)}g_{k,\,\mathrm{ideal}}^{(i,j)}\left(f_{d,k}+y\cdot\Delta f,R_k\right)}{\sigma^2}\right)\cdot
$$

$$
\exp\left\{-\frac{\left(\left|z_k^{(i+y,j)}\right|^2 - \left|z_k^{(i,j)}\right|^2\right) + \left|g_{k,\,\mathrm{ideal}}^{(i,j)}\left(f_{d,k}+y\cdot\Delta f,R_k\right)\right|^2}{\sigma^2}\right\}\mathrm{d}y. \quad (20)
$$

4. The proposed SPF algorithm

Based on the modelled LRF for defocused target, a novel SPF algorithm is proposed for target detection using the defocused image frame data. Unlike the traditional PF, a spawning particle set is generated by the target state particles, and $L_{\mathrm{def}}\left(z_k|\boldsymbol{x}_k,e_k\right)$ is used for updating. And an amplitude estimation method is also presented for reducing the sampling dimension.

4.1 Traditional PF

Assume that $\{\boldsymbol{x}_{0:k}^n;w_k^n\}_{n=1}^N$ represents N independent particles $\{\boldsymbol{x}_{0:k}^n, n=1,2,\cdots,N\}$ distributed with weights w_k^n which are generated by the posterior PDF $p(\boldsymbol{x}_{0:k}|\boldsymbol{z}_{1:k})$, then the true PDF can be expressed [24] based on Dirac function $\delta(\cdot)$:

$$
p(\boldsymbol{x}_{0:k}|\boldsymbol{z}_{1:k}) \approx \sum_{n=1}^N w_k^n\delta(\boldsymbol{x}_{0:k}-\boldsymbol{x}_{0:k}^n). \quad (21)
$$

In general, it is impossible to get the particles from the posterior PDF $p(\boldsymbol{x}_{0:k}|\boldsymbol{z}_{1:k})$ directly. Based on the importance sampling technology, a practical way is generating those particles from a proposal distribution $q(\boldsymbol{x}_{0:k}|\boldsymbol{z}_{1:k})$,. Then, the weight w_k^n of the ith particle is

$$
w_k^n = \frac{p(\boldsymbol{x}_{0:k}^n|\boldsymbol{z}_{1:k})\,p(\boldsymbol{x}_{0:k}^n)}{q\left(\boldsymbol{x}_{0:k}^n|\boldsymbol{z}_{1:k}\right)}. \quad (22)
$$

Then, based on sequential importance sampling, $q(\boldsymbol{x}_{0:k}^n|\boldsymbol{z}_{1:k})$ can be rewritten as

$$
q(\boldsymbol{x}_{0:k}|\boldsymbol{z}_{1:k}) = q(\boldsymbol{x}_k|\boldsymbol{x}_{0:k-1},\boldsymbol{z}_{1:k})q(\boldsymbol{x}_{0:k-1}|\boldsymbol{z}_{1:k-1}). \quad (23)
$$

The target state and system measurement generally satisfy the following requirement:

$$
\begin{cases}
p(\boldsymbol{x}_{0:k}) = p(\boldsymbol{x}_0)\prod_{m=1}^k p(\boldsymbol{x}_m|\boldsymbol{x}_{m-1})\\[2mm]
p(\boldsymbol{z}_{1:k}|\boldsymbol{x}_{0:k}) = \prod_{m=1}^k p(\boldsymbol{z}_m|\boldsymbol{x}_m)
\end{cases}. \quad (24)
$$

Hence, based on (23) and (24), (22) can be rewritten in recursive updating form [24] as follows:

$$
w_k^n = w_{k-1}^n\frac{p(\boldsymbol{x}_k^n|\boldsymbol{x}_k^{n-1})\,p(\boldsymbol{z}_k|\boldsymbol{x}_k^n)}{q(\boldsymbol{x}_k^n|\boldsymbol{x}_{k-1}^n,\boldsymbol{z}_k)}. \quad (25)
$$

Finally, the posterior filtered density $p(\boldsymbol{x}_k|\boldsymbol{z}_{1:k})$ can be approximated by

$$
p(\boldsymbol{x}_k|\boldsymbol{z}_{1:k}) \approx \sum_{n=1}^N w_k^n\delta\left(\boldsymbol{x}_k-\boldsymbol{x}_k^i\right). \quad (26)
$$

Equations (21)−(26) form the basis of PF [24].

4.2 SPF algorithm and its SMC implementation for defocused MTD

Based on the amplitude estimation and the deduced LRF of the defocused target, a novel SPF is proposed for MTD in this section. In the proposed method, two particle sets with associated weights $\{\boldsymbol{x}_k^n;w_k^n\}_{n=1}^N$ and $\left\{\boldsymbol{y}_k^{n,(s)}\right\}_{s=1}^{N_s}$ are used to calculate the density and LRF. Here, the nth particle $\boldsymbol{x}_k^n$ represents the target state, which is $\boldsymbol{x}_k^n = \left[A_k^n,R_k^n,f_{d,k}^n,f_{r,k}^n\right]$, and the spawning particle $\boldsymbol{y}_k^{n,(s)}$ is born in proximity to its parent particle $\boldsymbol{x}_k^n$ and thus its initial state depends on the parent's state. As presented in Subsection 3.2, the moving target is only defocused along the Doppler domain. Therefore, these new spawning particles are sampled in the Doppler domain, which can be modelled as $\boldsymbol{y}_k^{n(s)} = \left[f_{d,k}^{n(s)}\right]$. Based on the PF and those two particle sets, the processing flow of the SMC implementation of the SPF is shown in Fig. 5, where seven stages are included.
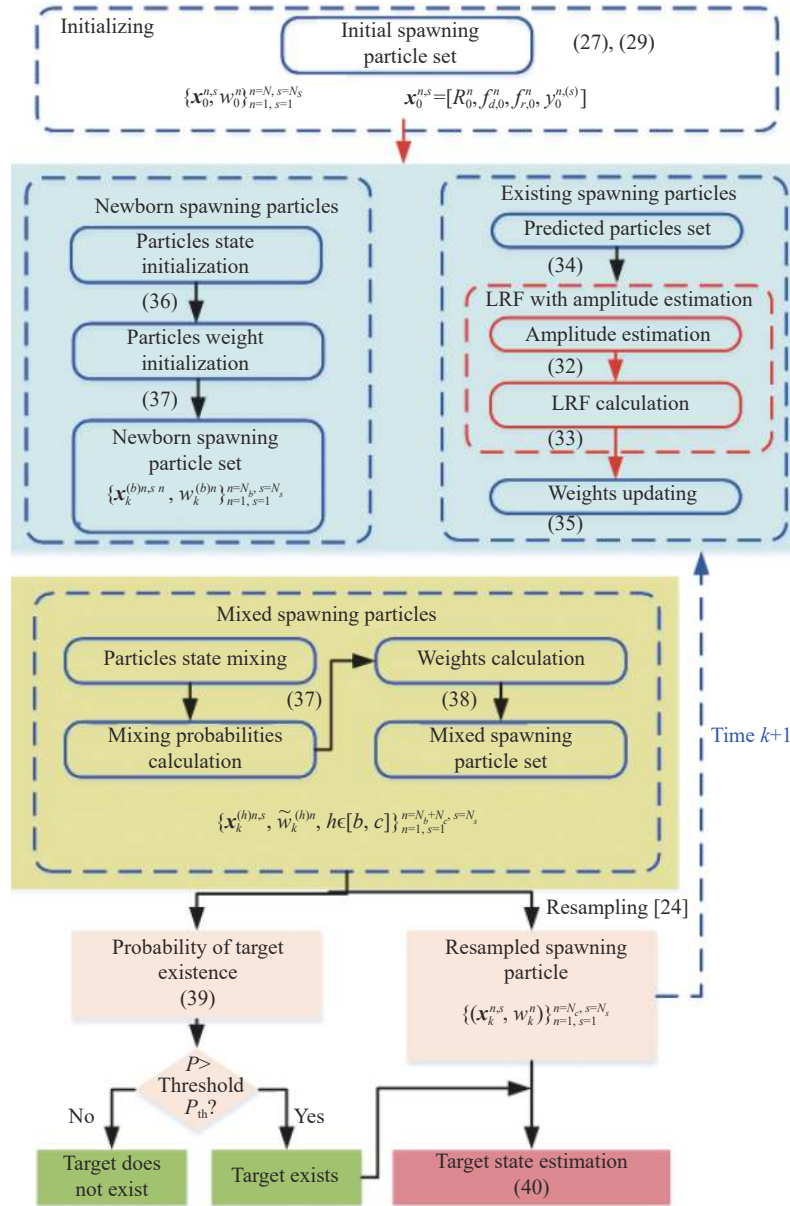
Fig. 5   Processing flow of the SMC implementation of the proposed SPF algorithm

4.2.1   Initialization

The first stage is initialization for generating the initial particle sets $\{x_0^n; w_0^n\}_{n=1}^N$ and $\{y_0^{n,(s)}\}_{s=1}^{N_s}$. The choice of the initial particle set plays an important role in the implementation of the proposed filter, which affects the efficiency of target detection and the number of particles required. In general, the uniform distribution is recommended, and the uniform particles can be drawn by

$$
\begin{cases}
R_0^n \sim \mathrm{U}[R_{\min} : \Delta R : R_{\max}] \\
f_{d,0}^n \sim \mathrm{U}[f_{\min} : \Delta f : f_{\max}] \\
f_{r,0}^n \sim \mathrm{U}[f_{r\min} : \Delta f_r : f_{r\max}] \\
f_{d,0}^{n(s)} \sim \mathrm{U}\left[f_d^n - L_{f,0}/2 \cdot \Delta f : \Delta f : f_d^n + L_{f,0}/2\right]
\end{cases} \tag{27}
$$

where $[R_{\min}, R_{\max}]$ is the range searching area, $[f_{\min}, f_{\max}]$ is the Doppler searching area, $[f_{r\min}, f_{r\max}]$ is the Doppler rate searching area, and the supporting length L_{f0} is decided by $f_{r,0}N_a/\mathrm{PRF}$. The discrete unit in range ΔR is decided by the signal sampling rate, the discrete unit in Doppler Δf can be calculated by PRF/N_a, and the discrete unit in Doppler rate Δf_r is decided by N_a or the frame duration T_s in each image frame. Considering the normalized amplitude reduction caused by Δf_r, as presented in (28), Fig. 6 shows the impact of Δf_r on amplitude reduction with different T_s, which equals N_a/PRF. Normally, T_s is around several seconds. Thus, the discrete unit in the Doppler rate Δf_r can be set less than 0.05 Hz/s.
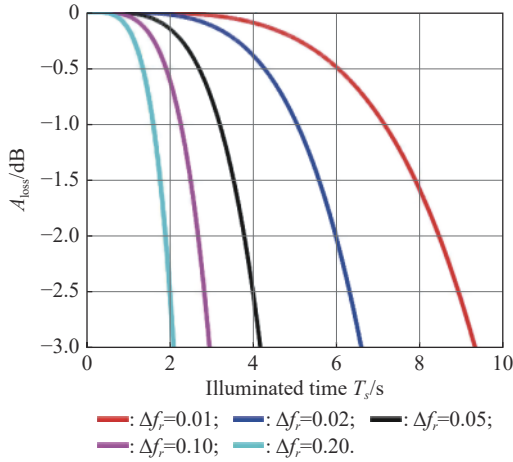
Fig. 6 Normalized amplitude reducing results caused by Δf_r

$$A_{\text{loss}} = \left| \sum_{m=-N_A/2}^{N_A/2-1} \exp\left\{ j\pi\Delta f_r(mT_p)^2 \right\} \right| \cdot N_a^{-1} \tag{28}$$

Based on the relationship between $fd_0^{n,(s)}$ and $f_{d,0}^n$, the way for the spawning particle to be generated in (27) can be rewritten as

$$\begin{cases} fd_0^{n,(s)} = fd_0^n + y_0^{(s)} \cdot \Delta f \\ y_0^{(s)} \sim U\left[\dfrac{-L_{f,0}}{2} : 1 : \dfrac{L_{f,0}}{2} \right] \end{cases} . \tag{29}$$

Therefore, the particle set $\{x_k^n\}_{n=1}^N$ and $\left\{y_k^{n,(s)}\right\}_{s=1}^{N_s}$ can be merged into a new spawning particle set $\{x_k^{n,s}, w_k^n\}_{n=1,s=1}^{n=N,s=N_s}$, where $x_k^{n,s} = \left[A_k^n, R_k^n, f_{d,k}^n, f_{r,k}^n, y_k^{n,(s)} \right]$, and the new set will be used in the following.

4.2.2 LRF with amplitude estimation

The second part is the calculation of LRF. For PF, the computing load is related to the dimension of target state, and the target amplitude sampling is also needed, which is only used for LRF calculation. In general, we are only interested in the position and velocity of a target. To avoid the amplitude sampling, an amplitude estimation method is proposed, which will improve the efficiency of the SPF. Moreover, the target state can be modelled as a 3D vector $x_k = [R_k, f_{d,k}, f_{r,k}]$, and the spawning particle $x_k^{n,s}$ is $\left[R_k^n, f_{d,k}^n, f_{r,k}^n, y_k^{n,(s)} \right]$.

In general, the first order approximation of Bessel function [37] is

$$I_0(x) \approx \frac{e^x}{\sqrt{2\pi x}}\left(1 + \frac{1}{8x} \right). \tag{30}$$

Then, the LRF in (12) can be rewritten as

$$L_{\text{ideal}}(z_k|x_k, e_k) \approx \prod_{i=1}^{N_{f\_s}} \prod_{j=1}^{N_{r\_s}} \exp\left\{ -\frac{A_k^2 \left| G_{k,\text{ideal}}^{(i,j)}(x_k) \right|^2}{\sigma^2} \right\} \cdot$$

$$\frac{\exp\left(\dfrac{2A_k z_k^{(i,j)} G_{k,\text{ideal}}^{(i,j)}(x_k)}{\sigma^2} \right)}{\sqrt{2\pi \cdot \dfrac{2A_k z_k^{(i,j)} G_{k,\text{ideal}}^{(i,j)}(x_k)}{\sigma^2}}} \cdot \left(1 + \frac{\sigma^2}{16 A_k z_k^{(i,j)} G_{k,\text{ideal}}^{(i,j)}(x_k)} \right) \tag{31}$$

where $G_{k,\text{ideal}}^{(i,j)}(x_k)$ is the normalization of $g_{k,\text{ideal}}^{(i,j)}(x_k)$. Using the principle of maximum likelihood estimation (MLE), the logarithm is applied on both sides of (31), and the partial derivative of A_k is

$$\frac{\partial \ln L_{\text{ideal}}(z_k|x_k, e_k)}{\partial A_k} \approx$$

$$-2A_k \sum_{i=1}^{N_{f\_s}} \sum_{j=1}^{N_{r\_s}} \frac{\left| G_{k,\text{ideal}}^{(i,j)}(x_k) \right|^2}{\sigma^2} + \sum_{i=1}^{N_{f\_s}} \sum_{j=1}^{N_{r\_s}} \frac{2z_k^{(i,j)} G_{k,\text{ideal}}^{(i,j)}(x_k)}{\sigma^2} -$$

$$\sum_{i=1}^{N_{f\_s}} \sum_{j=1}^{N_{r\_s}} \left(\frac{1}{2A_k} + \frac{1}{16A_k^2} \frac{\sigma^2}{z_{k,i}^{(i,j)} G_{k,\text{ideal}}^{(i,j)}(x_k)} \right). \tag{32}$$

Set (32) to 0, and the MLE $\hat{A}_k$ of A_k can be estimated by finding the solution to $\dfrac{\partial \ln L_{\text{ideal}}(z_k|x_k, e_k)}{\partial A_k} = 0$. Therefore, the LRF can be calculated by

$$L_{\text{def}}(z_k|x_k^{n,s}, e_k) = \prod_{i=1}^{N_{f\_s}} \prod_{j=1}^{N_{r\_s}} \frac{1}{L_f \cdot z_k^{(i,j)}} \cdot \exp\left\{ \frac{\left| z_k^{(i,j)} \right|^2}{\sigma^2} \right\} \cdot$$

$$\sum_{s=1}^{N_s} z_k^{(i+y_k^{n(s)}, j)} I_0\left(\frac{2z_k^{(i+y_k^{j(s)}, j)} \hat{A}_k G_{k,\text{ideal}}^{(i,j)}\left(f_{d,k}^{n(s)}, R_k \right)}{\sigma^2} \right) \cdot$$

$$\exp\left\{ -\frac{\left| z_k^{(i+y_k^{n(s)}, j)} \right|^2 + \hat{A}_k^2 \left| G_{k,\text{ideal}}^{(i,j)}\left(f_{d,k}^{n(s)}, R_k \right) \right|^2}{\sigma^2} \right\}. \tag{33}$$

4.2.3 Existing spawning particles

The existing spawning particles indicate that the target exists at both time $k-1$ and k, and they are generated by updating the N_c spawning particles at $k-1$ to k, based on the target state updating equation $x_k = Fx_{k-1} + v_k$, where v_k is the Gaussian distributed noise, and F is the state transition matrix:

$$F = \begin{bmatrix} 1 & \lambda T_s & \dfrac{\lambda T_s^2}{2} \\ 0 & 1 & T_s \\ 0 & 0 & 1 \end{bmatrix}. \tag{34}$$

The continuous particles at k are $\left\{x_k^{(c)n,s}\right\}_{n=1,s=1}^{n=N_c,s=N_s}$, where

the superscript (c) means continuous particle. Then, the normalized weights of continuous particles can be calculated by the LRF:

$$w_k^{(c)n} = \frac{L_{\text{def}}\left(z_k|x_k^{(c)n,s}, e_k\right)}{\sum\limits_{n=1}^{N_c} L_{\text{def}}\left(z_k|x_k^{(c)n,s}, e_k\right)}. \tag{35}$$

Therefore, the continuous spawning particle set with weights can be modelled as $\left\{x_k^{(c)n,s}, w_k^{(c)n}\right\}_{n=1,s=1}^{n=N_c,s=N_s}$.

4.2.4 Newborn spawning particles

The newborn spawning particles indicate that the target does not exist at time $k-1$ but exists at time k, and they are sampled from the proposal density

$$x_k^{(b)n,s} \sim q(x_k|e_k, \bar{e}_{k-1}, z_k), \quad \{i = 1, \cdots, N_b\}$$

$$w_k^{(b)n} =$$

$$\frac{L_{\text{def}}\left(z_k|x_k^{(b)n,s}, e_k\right) p\left(x_k^{(b)n,s}|e_k, \bar{e}_{k-1}\right)/q\left(x_k^{(b)n,s}|e_k, \bar{e}_{k-1}, z_k\right)}{\sum\limits_{n=1}^{N_b} L_{\text{def}}\left(z_k|x_k^{(b)n,s}, e_k\right) p\left(x_k^{(b)n,s}|e_k, \bar{e}_{k-1}\right)/q\left(x_k^{(b)n,s}|e_k, \bar{e}_{k-1}, z_k\right)}. \tag{36}$$

Therefore, the birth spawning particle set with weights can be modelled as $\left\{x_k^{(b)n,s}, w_k^{(b)n}\right\}_{n=1,s=1}^{n=N_b,s=N_s}$.

4.2.5 Mixed spawning particles

At the mixed spawning particle set stage, the mixing probabilities are calculated firstly, based on the $w_k^{(b)n}$ and $w_k^{(c)n}$, which are

$$\begin{cases} M_b = \dfrac{p(e_k|\bar{e}_{k-1})\, p(\bar{e}_{k-1}|z_{1:k-1}) \sum\limits_{n=1}^{N_b} w_k^{(b)n}}{p(e_k|\bar{e}_{k-1})\, p(\bar{e}_{k-1}|z_{1:k-1}) \sum\limits_{n=1}^{N_b} w_k^{(b)n} + p(e_k|e_{k-1})\, p(e_{k-1}|z_{1:k-1}) \sum\limits_{n=1}^{N_c} w_k^{(c)n}} \\[4mm] M_c = \dfrac{p(e_k|e_{k-1})\, p(e_{k-1}|z_{1:k-1}) \sum\limits_{n=1}^{N_c} w_k^{(c)n}}{p(e_k|\bar{e}_{k-1})\, p(\bar{e}_{k-1}|z_{1:k-1}) \sum\limits_{n=1}^{N_b} w_k^{(b)n} + p(e_k|e_{k-1})\, p(e_{k-1}|z_{1:k-1}) \sum\limits_{n=1}^{N_c} w_k^{(c)n}} \end{cases} \tag{37}$$

where $p(\bar{e}_{k-1}|z_{1:k-1})$ and $p(e_{k-1}|z_{1:k-1})$ denote the probability of target non-existing and existing at $k-1$, respectively. $p(e_k|\bar{e}_{k-1})$ and $p(e_k|e_{k-1})$ denote the probability of target appearance and target survival, respectively. Then, the birth spawning particle set and continuous spawning particle set are merged into a new mixed spawning particle set $\left\{x_k^{(h)n,s}, \tilde{w}_k^{(h)n}, h \in [b, c]\right\}_{n=1,s=1}^{n=N_b+N_c,s=N_s}$, and it should be noted that the weights of the mixing spawning particle set are normalized:

$$\begin{cases} \tilde{w}_k^{(b)n} = M_b w_k^{(b)n} \bigg/ \sum\limits_{n=1}^{N_b} w_k^{(b)n} \\[3mm] \tilde{w}_k^{(c)n} = M_c w_k^{(c)n} \bigg/ \sum\limits_{n=1}^{N_c} w_k^{(c)n} \end{cases}. \tag{38}$$

4.2.6 Resampling [24]

Resampling is an effective method to mitigate the degeneracy problem in the SMC implementation of PF. The main idea of resampling is that if the effective sample number is larger than a threshold, resampling is then performed. Resampling eliminates particles with low importance weights and multiplies particles of high importance. Based on resampling, the number of spawning particles is

resampled from N_b+N_c down to N_c, and the resampled spawning particle set is $\{(x_k^{n,s}, w_k^n), w_k^n = 1/N_c\}_{n=1,s=1}^{n=N_c,s=N_s}$.

4.2.7 Target state estimation

In the final stage, the probability of target existence can be calculated [35] by the mixing probabilities:

$$p(e_k|z_{1:k}) = \frac{M_b + M_c}{M_b + M_c + p(\bar{e}_k|e_{k-1})\, p(e_{k-1}|z_{1:k-1}) + p(\bar{e}_k|\bar{e}_{k-1})\, p(\bar{e}_{k-1}|z_{1:k-1})}. \tag{39}$$

If $p(e_k|z_{1:k})$ is over the threshold value P_{th}, the target is declared present, and its estimated state can be

$$\hat{x}_k = \sum\limits_{n=1}^{N_c} w_k^n x_k^n. \tag{40}$$

5. Experimental results and performance analysis

In this section, compared with the traditional PF algorithm, numerical simulations are carried out firstly to demonstrate the performance of the proposed SPF algorithm and its feasibility for defocused MTD. Then, some

preliminary experimental results are provided to show its performance in a practical scenario.

5.1　Results using simulated data

In the GBPR simulation system, the L5 signal from a GPS satellite (space vehicle number, SVN #10) is employed. Assume the target moves on the *XOY* plane, and the main simulation parameters are listed in Table 1, where 13 image frames are generated using the RFT imaging algorithm without Doppler rate compensation [38], and each frame illumination time T_s

is 5 s. The moving target appears at frame-3 and disappears at frame-11 with a constant velocity (100, −173, 0) m/s, and based on the system geometry, f_{dm} and f_{rm} caused by target motion can be calculated, which are 166.3 Hz and 1.01 Hz/s at frame-7. In Fig. 7, imaging results at frame-4 and frame-9 are presented, and to highlight the target, all image frames in Fig. 7 are noise-free. As shown, the target is defocused in the Doppler domain, and due to target motion, the defocused target is located in different RD cells at different image frames.

Table 1　Main simulation parameters

Parameter	Value	Parameter	Value
Wavelength/m	0.255	Supporting length $L_{f,0}$/pixel	40
Antenna gain/dB	30	Spawning particles number N_s	400
Target appearance	Frame-3	Continuous/born particles number $N_c=N_b$	10 000
Target disappearance	Frame-11	Target position/km	(100,100,8)
Threshold P_{th}	0.5	Target velocity/(m·s^{-1})	(100,−173,0)
Image frames	13	Image SNR/dB	8, 10
Target RCS/dB	30	SVN #10 position/km	(10 232.9, −15 519.5, 12 420.5)
Sampling rate/MHz	50.0	SVN #10 Velocity/(m·s^{-1})	(190.2, −2 114.0, −1 798.6)
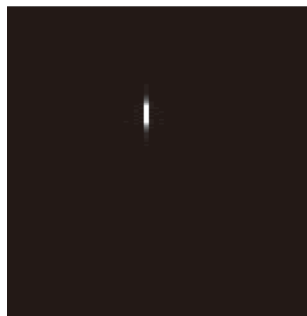
(a) Frame-4
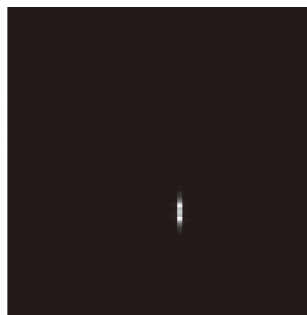
(b) Frame-9

Fig. 7　Noise-free simulated image frame results

For both traditional PF and proposed SPF, the initial target state is generated by the uniform distribution, where $R_0\sim U[−1\,000,1\,000]$ m (the reference range is

removed), $f_{d,0}\sim U[100,220]$ Hz, $f_{r,0}\sim U[0,1.5]$ Hz/s, and $y_0\sim U[−20,20]$. The processing results of each image frame are shown as the distribution of 'alive' particle clouds (red points) in Fig. 8, where the blue circle marks the true target position at the current frame, and the black line represents the target trajectory in the RD plane from frame-3 to frame-11. Those particles appear randomly dispersed at the beginning of target appearance, but as the PF-based method can learn from the image data the presence and location of this moving target, when more image frames are used, the particle clouds become more and more concentrated around the true location. In the traditional PF, the LRF model is not matched with the response function of the defocused target. As shown in Fig. 8(a), the particle clouds are randomly distributed in the image area, and even after several image frames, as shown in Fig. 8(c), the particle clouds are just a little bit concentrated around the true target location and still condensed to a slanted line in the Doppler direction. This phenomenon indicates that the traditional LRF is not matched in the Doppler domain. As a result, it is difficult for the traditional PF to detect and track the defocused moving target. As shown in Fig. 8(b), for the proposed SPF, the particle clouds have been focused to a line in the Doppler direction and MTD has been preliminarily realized. However, the error of the estimated state is still

large, which is due to error of the modified LRF model as amplitude estimation is not accurate enough at the beginning. Then, as shown in Fig. 8 (d), with the increase of input image frame data, the accuracy of target amplitude

estimation and LRF model is gradually improved, and particle clouds become more concentrated towards the true target position. Finally, the estimated target trajectory can be obtained based on the estimation target state.
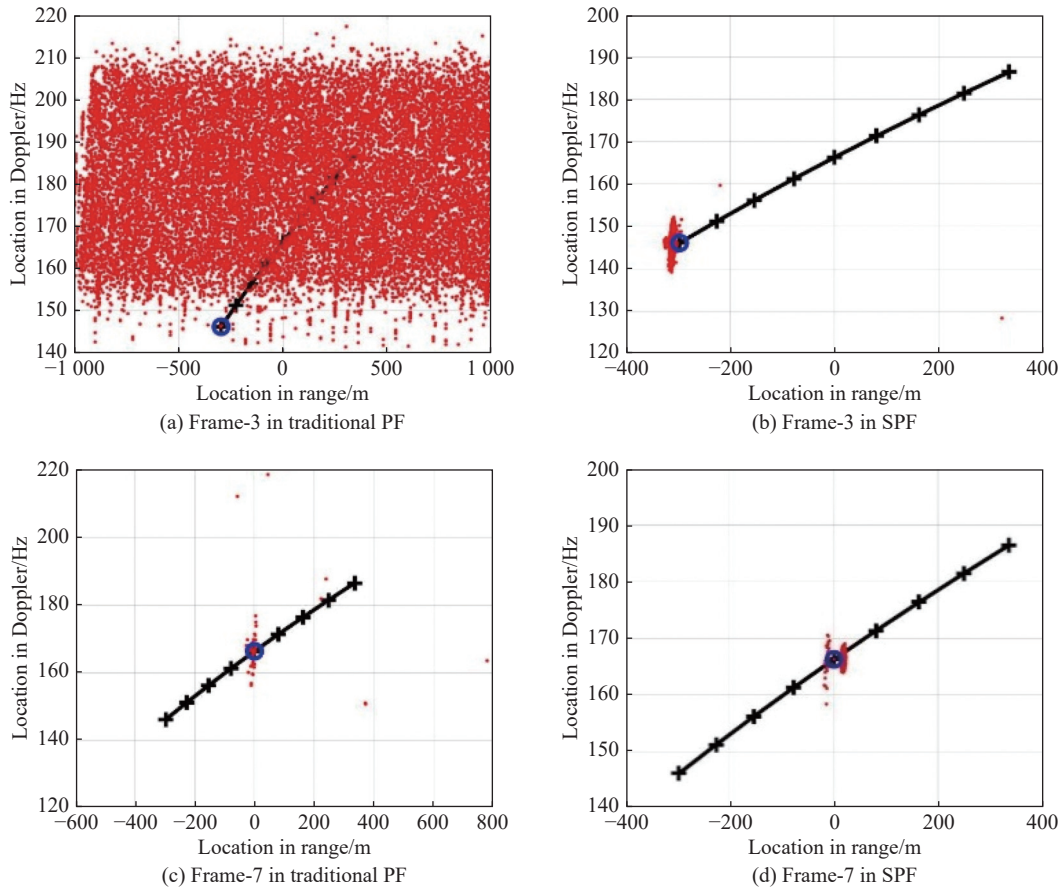

(a) Frame-3 in traditional PF

(b) Frame-3 in SPF

(c) Frame-7 in traditional PF

(d) Frame-7 in SPF

Fig. 8   Locations of particle clouds after filtering at each frame with a 10 dB image SNR

The true and estimated trajectories in the RD image are shown in Fig. 9, where the target moves from bottom left to top right. For the traditional PF, the target cannot be detected at the beginning, and then with more frames, the target is detected but the estimated track error is too large. However, for the SPF, as shown by the red line in Fig. 9, the target is detected when it appears, and the estimated track becomes close to the true one gradually. In the simulation, conducted on a computer with intel core i-7-6820HQ@2.70 GHz processors, the SPF has competitive advantages compared with the traditional PF. The traditional PF takes 39.05 s to process, while SPF shows relatively same speedy processing time with 41.66 s, in consideration of the overall effects of introduced additional spawning particles and reduction of the sampling dimension.
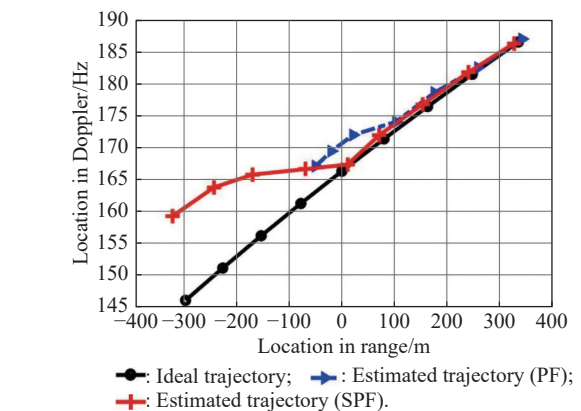

Fig. 9   Target detection results by the traditional PF and the proposed SPF algorithm

Next, 500 Monte Carlo simulations are carried out to evaluate the performance of the proposed SPF, in terms of detected frame rate, root mean square (RMS) Doppler

estimation error and RMS range estimation error [38]. The detected frame rate results are shown in Fig. 10, with a $P_{th} = 0.5$ to determine whether the target is detected or not. As shown, a higher detected frame rate is obtained when the image SNR is high, and the detected frame rate by the SPF (red and blue line) is much higher than that by the traditional PF given the same image quality, which verifies effectiveness of the proposed SPF. Moreover, although the detected frame rate is low at the beginning when the target appears, the PF and SPF algorithms can learn target information from the image data, and as more image frames are used for MTD, the detected frame rate increases dramatically.
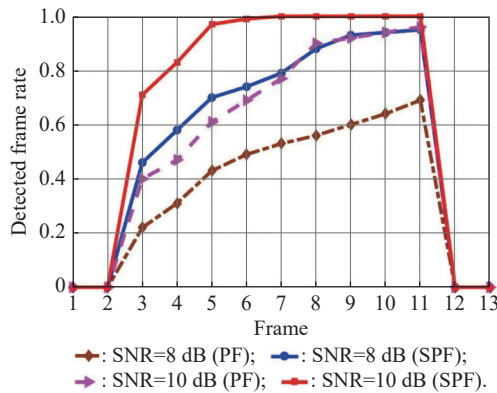

Fig. 10   Detected frame rate result by the traditional PF and the proposed SPF algorithm with different image SNRs

In Fig. 11, the RMS estimation error results of the target Doppler and range are presented, where both errors are large at the beginning, but they become smaller with the increase of image frames. Same as in Fig. 10, the RMS estimation error in the SPF case (red and blue line) is much smaller than that in the traditional PF case, and a lower RMS estimation error is obtained with a higher image SNR. In our simulations, the range resolution is around 10 m and the Doppler resolution is 0.2 Hz ($1/T_s$). As shown by the red line in Fig. 11, the final RMS estimation error of target range and Doppler is close to the ideal resolution, which demonstrates that the proposed SPF can track the target accurately.
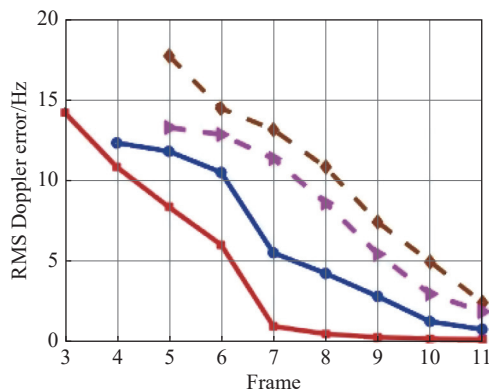
(a) RMS error of Doppler
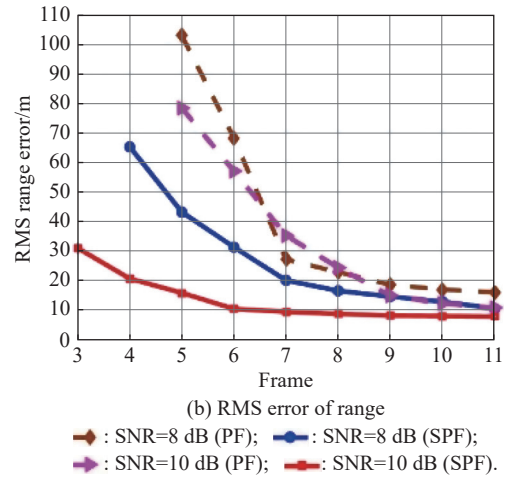
(b) RMS error of range

→ : SNR=8 dB (PF);   → : SNR=8 dB (SPF);
→ : SNR=10 dB (PF);   → : SNR=10 dB (SPF).

Fig. 11   RMS estimation error in different image SNR cases

5.2   Preliminary experimental results with GPS signals

To demonstrate the effectiveness of the proposed SPF in a practical scenario, a preliminary experiment was conducted near the Beijing Capital Airport (PEK), China at 19:48:20 (local time) on 31 May 2021, and the experimental scene and hardware setups are shown in Fig. 12, where the reference and receiver antennas are fixed on the blue spot, and the receiver antenna points to the vertical direction (almost West) of the target trajectory. In the experiment, the flight CA1902 from Urumqi to Beijing was landing from South to North at a speed of 78 m/s, GPS satellites SVN #02, #13, and #30 are chosen as the transmitters and the L1 signal (corresponding resolution is around 150 m) is chosen as the illumination source. At this situation, the flight can be regarded as a point target. More details about the experimental parameters are listed in Table 2. Note that the positions of targets, satellites and receivers are recorded in the Earth-Centered Earth-Fixed (ECEF) coordinate at reference time (19:48:20), and the range between flight and receiver at reference time R_R is around 1.21 km.


(a) Experimental scene

(b) Hardware setup
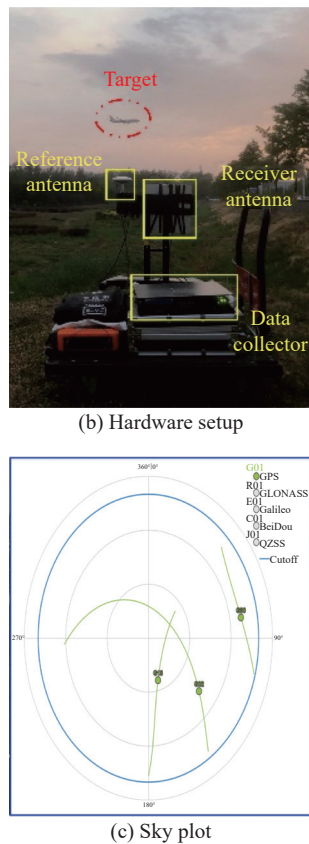
(c) Sky plot

Fig. 12   Illustration of the experimental scene, hardware setups and corresponding sky plot

Table 2   Experimental parameters with GPS satellites

Parameter	Value
Wavelength/m	0.19
Sampling rate/MHz	62
Signal bandwidth/MHz	2.046
Antenna gain/dB	15
Target speed/$(m \cdot s^{-1})$	78
SVN #02 position/km	$(-21\,605.1, 14\,765.4, 5\,351.2)$
SVN #13 position/km	$(-13\,120.6, 20\,485.8, 10\,363.6)$
SVN #30 position/km	$(-23\,221.1, -1\,572.9, 13\,072.6)$
Receiver position/km	$(-2\,191.8, 4\,370.8, 4\,081.2)$
Target position/km	$(-2\,191.3, 4\,371.9, 4\,081.6)$

Based on the signal synchronization algorithm [3] and RFT algorithm [36], eight frames of RD image result are

generated for each transmitter (SVN #02, #13, and #30). The illumination time of each frame is 0.5 s, and the frame time interval is 0.2 s. Thus, the total illumination time is very short (1.6 s), and the flight can be assumed to be moving at a constant speed in the process. It can also be assumed that it is moving on the *XOY* plane, because the average vertical flight velocity during landing is just around 2 m/s. For illustration, frame-2 and frame-5 under the geometry of SVN #13 are shown in Fig. 13. As shown, the target is defocused along the Doppler direction, as the QPE caused by Doppler rate is not compensated. Both the Doppler frequency introduced by the GPS satellite motion and the reference range have been removed. Considering the prior information about the flight, the initial target state is generated by uniform distribution, where $R_0 \sim U[0, 3\,000]$ m, $f_{d,0} \sim U[-100, 100]$ Hz, $f_{r,0} \sim U[15, 20]$ Hz/s, and $y_0 \sim U[-10, 10]$. The other SMC implementation parameters are the same as those listed in Table 1. Since the RD history of each geometry configuration is totally different, the same target will be located in different RD cells if a different transmitter is used. Therefore, three estimated tracks (blue for SVN #02, red for SVN #13, pink for SVN #30) are obtained, as shown in Fig. 14. For the reference time, the estimated target Doppler and range parameter are listed in Table 3. Then, based on the relationship between a target's position, speed and RD parameter [35], the position and speed of the detected flight can be estimated using parameters listed in Table 3, which gives the flight position at $(-2\,191.27, 4\,371.86, 4\,081.61)$ km with an estimated speed of 76.4 m/s, while the estimated R_R is around 1.23 km. All these again have demonstrated the effectiveness of the proposed SPF.
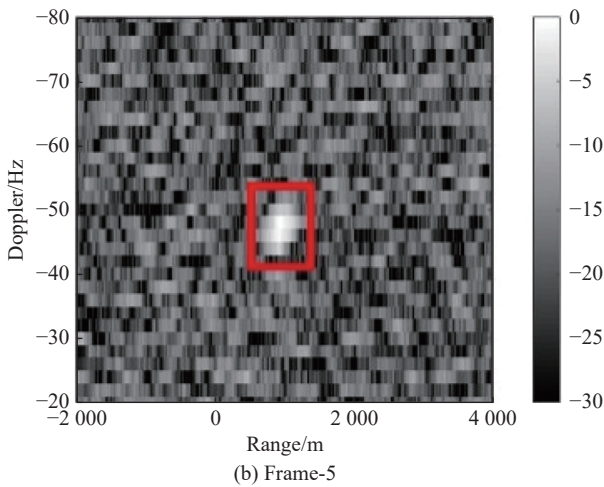

(a) Frame-2

(b) Frame-5
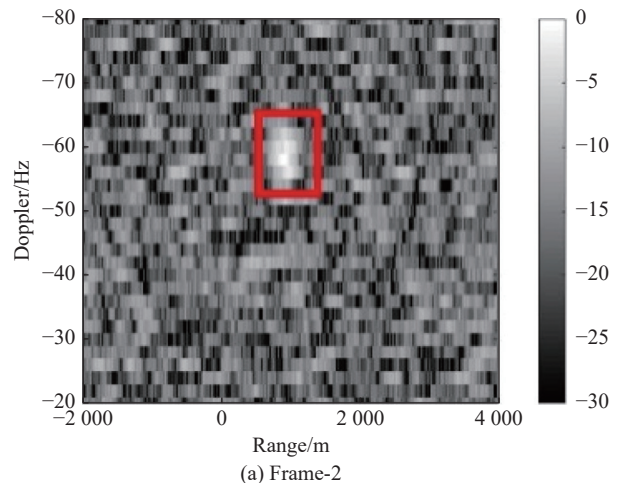
Fig. 13   RD image using SVN #13 as the transmitter

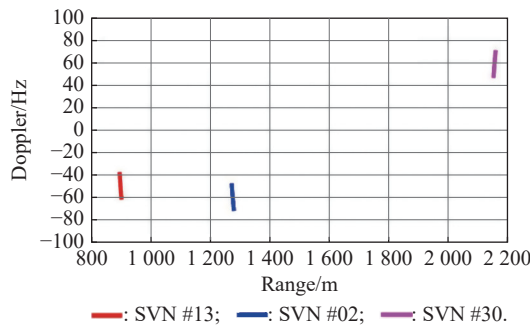—: SVN #13;   —: SVN #02;   —: SVN #30.

Fig. 14   Estimated target tracks in range-Doppler plane

Table 3   Estimated target information at the reference time

Satellite	Doppler/Hz	Range/m
SVN #02	−72.2	1 280
SVN #13	−61.9	907
SVN #30	46.3	2 149

6. Conclusions

In this paper, the defocused point-like target detection in GBPR system has been studied. To detect the defocused target, the measurement model and the modified LRF model are first derived to describe the target data, which can also be applied to detection of multiple targets in single-static or multi-static GBPR systems. Then, a novel SPF algorithm and its SMC implementation are proposed, where a spawning particle set generation method is developed with reference to the traditional particles in PF as their parent. To reduce the sampling dimension and computation in SMC implementation, a novel amplitude estimation method based on the modified LFR is presented. After that, spawning particles initializing, LRF calcula-

tion, newborn and existing spawning particles calculation, mixed spawning particle set generation, resampling, and target state estimation are presented to make full use of all image frame data to realize the defocused MTD. As demonstrated by numerical simulations and preliminary experimental results, the proposed algorithm can realize high-precision defocused MTD, with an error just around the resolution cell size. Comparing with the traditional PF, the computation efficiency of the proposed SPF is almost the same, due to the reduction of the sampling dimension. Moreover, due to the availability of multiple GNSS satellites, multiple observations from different transmitters allow the proposed algorithm to effectively obtain not only the range and Doppler parameters of the moving target but also its position and velocity. Based on findings in this paper, our next work is to explore the extended moving target detection with real GBPR data.

References

[1] ZAVOROTNY V U, GLEASON S, CARDELLACH E, et al. Tutorial on remote sensing using GNSS bistatic radar of opportunity. IEEE Geoscience and Remote Sensing Magazine, 2014, 24(4): 8–45.

[2] LI W Q, CARDELLACH E, RIBO S, et al. First spaceborne demonstration of BeiDou-3 signals for GNSS reflectometry from CYGNSS constellation. Chinese Journal of Aeronautics, 2021, 34(9): 1–10.

[3] SADEGHI M, BEHNIA F, AMIRI R. Maritime target localization from bistatic range measurements in space-based passive radar. IEEE Trans. on Instrumentation and Measurement, 2021, 70: 8502708.

[4] ANTONIOU M, CHERNIAKOV M. GNSS-based bistatic SAR: a signal processing view. EURASIP Journal on Advances in Signal Processing, 2013, 1: 98.

[5] ANTONIOU M, ZENG Z, LI F F, et al. Experimental demonstration of passive BSAR imaging using navigation satellites and a fixed receiver. IEEE Geoscience and Remote Sensing Letters, 2012, 9(3): 477–481.

[6] ZHOU X K, CHEN J, WANG P B, et al. An efficient imaging algorithm for GNSS-R bi-static SAR. Remote Sensing, 2019, 11(24): 2945.

[7] LIU F, FAN X Z, ZHANG T, et al. GNSS-based SAR interferometry for 3-D deformation retrieval: algorithms and feasibility study. IEEE Trans. on Geoscience and Remote Sensing, 2018, 56(10): 5736–5748.

[8] ZHANG Q L, ANTONIOU M, CHANG W G, et al. Spatial decorrelation in GNSS-based SAR coherent change detection. IEEE Trans. on Geoscience and Remote Sensing, 2015, 53(1): 219–228.

[9] HE Z Y, YANG Y, CHEN W. A hybrid integration method for moving target detection with GNSS-based passive radar. IEEE Journal of Selected Topics in Applied Earth Observations and Remote Sensing. 2021, 14: 1184−1193.

[10] ZENG H C, CHEN J, WANG P B, et al. Moving target detection in multi-static GNSS-based passive radar based on multi-bernoulli filter. Remote Sensing, 2020, 12(21): 3495.

[11] MA H, ANTONIOU M, STOVE A G, et al. Target kinematic state estimation with passive multistatic radar. IEEE Trans. on Aerospace and Electronic Systems, 2021, 57(4): 2121–2134.

[12] PASTINA D, SANTI F, PIERALICE F, et al. Passive radar imaging of ship targets with GNSS signals of opportunity. IEEE Trans. on Geoscience and Remote Sensing, 2021, 59(3): 2627–2642.

[13] MA H, ANTONIOU M, PASTINA D, et al. Maritime moving target indication using passive GNSS-based bistatic radar. IEEE Trans. on Aerospace and Electronic Systems, 2018, 54(1): 115–130.

[14] ZHOU X K, WANG P B, ZENG H C, et al. Moving target detection using GNSS-based passive bistatic radar. IEEE Trans. on Geoscience and Remote Sensing, 2022, 60: 5113415.

[15] HE X, ZENG T, CHERNIAKOV M. Signal detectability in SS-BSAR with GNSS non-cooperative transmitter. IEE Proceedings-Radar Sonar and Navigation, 2005, 152(3): 124–132.

[16] TAO R, ZHANG N, WANG Y C. Analyzing and compensating the effects of range and Doppler frequency migrations in linear frequency modulation pulse compression radar. IET Radar Sonar & Navigation, 2011, 5(1): 12–22.

[17] XU J, YU J, PENG Y N, et al. Radon-Fourier transform for radar target detection, I: generalized Doppler filter bank. IEEE Trans. on Aerospace and Electronic Systems, 2011, 47(2): 1186–1202.

[18] BELTRAMONTE T, BRACE P, BISCEGLIE M D, et al. Simulation-based feasibility analysis of ship detection using GNSS-R delay-Doppler maps. IEEE Journal of Selected Topics in Applied Earth Observations and Remote Sensing, 2020, 13: 1385–1399.

[19] ZHOU X K, WANG P B, CHEN J, et al. A modified Radon Fourier transform for GNSS-based bistatic radar target detection. IEEE Geoscience and Remote Sensing Letters, 2022, 19: 3501805.

[20] XU J, YU J, PENG Y N, et al. Radon-Fourier transform for radar target detection (II): blind speed sidelobe suppression. IEEE Trans. on Aerospace and Electronic Systems, 2011, 47(4): 2473–2486.

[21] YU J, XU J, PENG Y N, et al. Radon-Fourier transform for radar target detection (III): optimality and fast implementations. IEEE Trans. on Aerospace and Electronic Systems, 2012, 48(2): 991–1004.

[22] CHEN X L, GUAN J, LIU N B, et al. Maneuvering target detection via Radon-fractional Fourier transform-based long-time coherent integration. IEEE Trans. on Signal Processing, 2014, 62(4): 939–953.

[23] RUTTEN M G, GORDON N J, MASKELL S. Recursive track-before-detect with target amplitude fluctuations. IEE Proceedings-Radarm-Sonar and Navigation, 2005, 152: 345–352.

[24] RISTIC B, ARULAMPALAM S, GORDON N. A beyond the Kalman filter: particle filters for tracking applications. Boston: Artech House, 2004.

[25] XU C, HE Z S, LIU H C, et al. Bayesian track-before-detect algorithm for nonstationary sea clutter. Journal of Systems Engineering and Electronics, 2021, 32(6): 1338–1344.

[26] SALMOND D J, BIRCH H. A particle filter for track before-detect. Proc. of the American Control Conference, 2001, 5: 3755–3760.

[27] ROLLASON M, SALMOND D J. A particle filter for track before-detect of a target with unknown amplitude. IEE Target Tracking: Algorithms and Applications, 2001. DOI: 10.1049/ic:20010240.

[28] MAHLER R. PHD filters of higher order in target number. IEEE Trans. on Aerospace and Electronic Systems, 2007, 43(4): 1523–1543.

[29] LI T C, CORCHADO J M, SUN S D, et al. Multi-EAP: extended EAP for multi-estimate extraction for SMC-PHD filter. Chinese Journal of Aeronautics, 2017, 30(1): 369–379.

[30] SI W J, ZHU H F, QU Z Y. Multi-sensor Poisson multi-Bernoulli filter based on partitioned measurements. IET Radar, Sonar & Navigation, 2020, 14(6): 860–869.

[31] SU Z Z, JI H B, ZHANG Y Q. A Poisson multi-Bernoulli mixture filter with spawning based on Kullback-Leibler divergence minimization. Chinese Journal of Aeronautics, 2021, 34(11): 154–168.

[32] YANG X J, XING K Y, FENG X L. Maneuvering target tracking in dense clutter based on particle filtering. Chinese Journal of Aeronautics, 2011, 24(2): 171–180.

[33] UBEDA-MEDINA L, GARCIA-FERNANDEZ A F, GRAJAL J. Adaptive auxiliary particle filter for track-before-detect with multiple targets. IEEE Trans. on Aerospace and Electronic Systems, 2017, 53(5): 2317–2330.

[34] FREITAS A D, MIHAYLOVA L, GNING A, et al. A box particle filter method for tracking multiple extended objects. IEEE Trans. on Aerospace and Electronic Systems, 2019, 55(4): 1640–1655.

[35] RUTTEN M, GORDON N, MASKELL S. Efficient particle-based track-before-detect in Rayleigh noise. Proc. of the 7th International Conference on Information Fusion, 2004: 693–700.

[36] ZENG H C, CHEN J, WANG P B, et al. 2-D coherent integration processing and detecting of aircrafts using GNSS-based passive radar. Remote Sensing, 2018, 10(7): 1164.

[37] OLIVARES J, MARTIN P, VALERO E. A simple approximation for the modified Bessel function of zero order $I_0(x)$. Journal of Physics Conference Series, 2018, 1043: 012003.

[38] GAO H, LI J W. Detection and tracking of a moving target using SAR images with the particle filter-based track-before-detect algorithm. Sensors, 2014, 14(6): 10829–10845.

Biographies

ZENG Hongcheng was born in 1989. He received his B.S. degree from China Agriculture University in 2011, Ph.D. degree in signal and information processing from Beihang University, Beijing, China, in 2016. Since 2019, He has been an assistant professor with the School of Electronics and Information Engineering, Beihang University. He was a visiting researcher with the School of Mathematics and Statistics, University of Sheffield, Sheffield, U.K., from 2017 to 2018. He has published more than 20 journal and conference papers. His research interests include high-resolution spaceborne synthetic aperture radar image formation, passive radar signal processing, and moving target detection.
E-mail: zenghongcheng@buaa.edu.cn

DENG Jiadong was born in 1995. He received his B.S. degree in information and computational science from Beihang University, Beijing, China, in 2017, where he is currently pursuing his Ph.D. degree in signal and information processing. His research interests include spaceborne synthetic aperture radar (SAR) image formation for terrain observation by progressive scans (TOPS) mode and sliding spotlight mode.
E-mail: djdong0725@buaa.edu.cn

WANG Pengbo was born in 1979. He received his Ph.D. degree in information and communication engineering from Beihang University, Beijing, China, in 2007. From 2007 to 2010, he held a postdoctoral position at the School of Electronics and Information Engineering, Beihang University. From 2014 to 2015, he was a visiting researcher with the Department of Electronic and Electrical Engineering, University of Sheffield, Sheffield, U.K. Since 2015, he has been an associate professor with the School of Electronics and Information Engineering, Beihang University. His research interests include high-resolution spaceborne synthetic aperture radar (SAR) image formation, novel techniques for spaceborne SAR systems, and multimodal remote sensing data fusion.
E-mail: wangpb7966@buaa.edu.cn
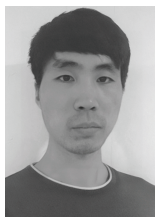
ZHOU Xinkai was born in 1992. He received his B.S. degree in electronic engineering from Beihang University, Beijing, China, in 2015, where he is currently pursuing his Ph.D. degree in signal and information processing. His research interests include active/passive synthetic aperture radar (SAR) image formation, Global Navigation Satellite System (GNSS)-based SAR, and GNSS-based moving target detection moving target detection radar.
E-mail: zhoux1nka1@buaa.edu.cn

YANG Wei was born in 1983. He received his M.S. and Ph.D. degrees in signal and information processing from Beihang University (BUAA), Beijing, China, in 2008 and 2011, respectively. From 2011 to 2013, he held a post-doctoral position at the School of Electronics and Information Engineering, Beihang University. Since July 2013, he has been with the School of Electronics and Information Engineering, BUAA as a lecturer. From 2016 to 2017, he researched as a visiting researcher with the Department of Electronic and Electrical Engineering, University of Sheffield, Sheffield, U.K. He has been an associate professor with the School of Electronics and Information Engineering, BUAA, since 2018. He has authored or co-authored more than 60 journal and conference publications. His research interests include moving target detection, high-resolution spaceborne synthetic aperture radar (SAR) image formation, SAR image quality improvement, and 3D imaging.
E-mail: yangweigigi@sina.com

CHEN Jie was born in 1973. He received his B.S. and Ph.D. degrees in information and communication engineering from Beihang University, Beijing, China, in 1996 and 2002, respectively. Since 2004, he has been an associate professor with the School of Electronics and Information Engineering, Beihang University. He was a visiting researcher with the School of Mathematics and Statistics, University of Sheffield, Sheffield, U.K., from 2009 to 2010, working on ionospheric effects on low-frequency space radars that measure forest biomass and ionospheric electron densities. Since July 2011, he has been a professor with the School of Electronics and Information Engineering, Beihang University. His research interests include multimodal remote sensing data fusion, topside ionosphere exploration with spaceborne high frequency/very high frequency-synthetic aperture radar (SAR) systems, and high-resolution spaceborne SAR image formation and SAR image quality enhancement.
E-mail: chenjie@buaa.edu.cn